INFLUENCE OF THERMAL DIFFUSE SCATTERING ON IMAGE CONTRAST IN SCANNING TRANSMISSION ELECTRON MICROSCOPY

M.D. Croitoru and D. Van Dyck

EMAT, University of Antwerp, 171, Groenenborgerlaan, B-2020, Antwerp, Belgium
(Received 29 March 2007)

Abstract

We analyze the loss of contrast in simulated atomic-resolution annular dark-field scanning transmission electron microscopy images due to the incoherent thermal diffuse scattering (TDS) for $SrTiO_3$ and $PbTiO_3$ samples. The contribution of TDS in the contrast reduction is evaluated within the TDS generation function approximation. From the thickness dependence of the contrast loss in simulated images it is seen that inclusion of thermal diffuse scattering leads to a strong reduction of the image contrast.
PACS numbers: 61.16.Bg; 87.64.Bx

1. Introduction

It is avowed that image contrast in transmission electron microscopy is usually less by a factor of approximately three than what image simulations predict. This strong contrast reduction in transmission electron microscopy (TEM) images is referred to as the Stobbs factor. The quantitative discrepancy, when matching a simulated sample image to an experimental one, was first pointed out in Refs. [1-3] and still is a subject of persisting interest in the microscopy community. The understanding of the reasons for a lack of agreement between experimental and simulated images got a further development in a relatively large number of works [4-8]. However the problem cannot be considered as being solved.

The study of the role of thermal diffuse scattering (TDS) in the image formation in the scanning transmission electron microscopy (STEM) mode attracted a lot of interest in the past. The importance of the TDS image formation comes from the fact that, whereas TDS scattering mechanism does not cause significant energy-loss of strongly accelerated electrons, it produces large momentum transfer, which can scatter the electrons to the angular range of the STEM annular dark-field (ADF) detector. Moreover, since the loss of image contrast was even observed after energy filtering of the image, the phonon scattering, or thermal diffuse scattered electrons can be considered as a possible cause of significant contrast reduction (perhaps, also in HRTEM imaging mode), since an energy filter can remove away most of the inelastically scattered electrons, but electrons with an energy loss smaller than 1 eV remain in the image formation process. For this purpose, several approaches have been developed in the past to simulate the image formation in STEM with inclusion of thermal diffuse scattering. In the "frozen phonon" model, first proposed in Ref. [9], a number of calculations is performed for various static configurations of atoms, slightly displaced from their mean positions. Then the image intensity is calculated by averaging the intensities obtained from different lattice configurations. According to Ref. [10], this method can be considered as the most accurate one, although it is quite time consuming. Wang and Cowley proposed a method based on the multislice formalism, which includes TDS within the first order approximation [10-12]. Dinges and Rose developed a semi-analytical approach within the multislice formalism [13].

Allen and Rossouw [14], Pennycook and Jesson [15] and Watanabe *et al*. [16] have incorporated TDS in the Bloch wave formalism. Allen *et al*. [17, 18] have modified the Bloch wave theory and multislice technique to account for the lattice-resolution contrast derived from both coherent and incoherent scattering mechanisms using a mixed dynamic form factor. The mixed dynamic form factor within the Einstein approximation for atom vibrations is derived in Ref. [19]. Muller et al. went beyond the Einstein approximation and simulated TDS including a detailed phonon dispersion curve [20].

The purpose of the present work is to study the influence of thermal diffuse scattering on the contrast reduction in the images of $SrTiO_3$ and $PbTiO_3$ specimens obtained in STEM mode with a high-angle annular dark-field (HAADF) detector. For this purpose we have employed the method developed in Ref. [21].

2. Theoretical model

In this work we use the multislice many-beam dynamic electron diffraction method, first proposed by Cowley and Moodie [22], to simulate dynamic electron scattering, since we intend to investigate atomic level resolution images. This method does not require three-dimensional periodicity of the crystal, and therefore it is more convenient than Bloch method [16, 23] proposed by Bethe in Ref. [24] to apply to study defects in crystals, such as displacements of atom positions in the frozen phonon model. Finally, the multislice method numerically suits more for the calculation of thickness-dependent characteristics, because the wave propagation through the crystal can be calculated slice-by-slice.

Primarily the multislice method was derived from the physical optics approach under the small-angle-scattering approximation neglecting backscattering. It also can be deduced from Feynman's path-integral formalism for high-energy electron diffraction (see Refs. [25, 26]) or directly from the Schrödinger equation [27]. The forward-scattering assumption for high-energy electrons is investigated and validated in Ref. [28]. The idea-algorithm of the multislice method can be described as follows. The crystal is divided into many parallel slices, as seen in Fig. 1(a). The scattering of each slice can be based on the projected potential approximation [29, 30], if the thickness of each slice is sufficiently small (Fig. 1(b)). If the backscattering effect is negligible, the transmission of the electron wave through each slice can be considered as a two-step process - the phase modulation of the wave by the projected atomic potential within the slice and the propagation of the modulated wave in a vacuum for the distance Δz along the beam direction before striking the next crystal slice (Fig. 1(c)). Labeling the wave function at the top of each slice by Ψ_n ($\rho = (x, y)$) and propagator and transmission functions for each slice by $P_n(\rho, \Delta z_n)$ and $T_n^0(\rho)$, respectively, the basic first-order multislice equation, describing the diffraction of the electron beam by the crystal as a consecutive slice-by-slice process up to the exit face of the specimen, can be written as [31, 32]:

$$\Psi_{n+1}(\rho) = P_n(\rho, \Delta z_n / 2) \otimes \left\{ T_n^0(\rho) \left[P_n(\rho, \Delta z_n / 2) \otimes \Psi_n(\rho) \right] \right\} + O(\Delta z^3), \tag{1}$$

where

$$P_n(\rho, \Delta z_n) = \frac{k_z}{i \Delta z_n} \exp\left[\frac{i \pi k \rho^2}{\Delta z_n} \right], \tag{2}$$

$$T_n^0(\rho) = \exp\left[i \sigma \frac{k}{k_z} \int_{z_n}^{z_{n+1}} V_n(\rho, z) dz \right] \equiv \exp\left[i \sigma U_n(\rho) \right], \tag{3}$$

with Δz_n the thickness of the n-th slice, $V_n(\rho, z)$ the potential field in the n-th slice and $\sigma = e/\hbar v$ an interaction parameter with v is the velocity of incident electron. It is possible to develop a second-order multislice theory by introducing potential eccentricity as described in Refs. [32, 33], but in the present work the z-dependence of the potential (for HOLZ) and the high accuracy of calculations are ensured by the small slice thickness.

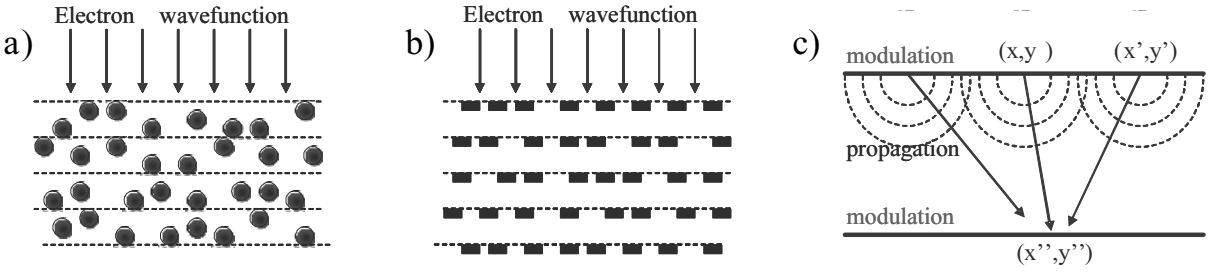

Fig. 1. The multislice method. a) The crystal is divided into many parallel slices. b) The potential field in each slice can be considered projected on the entrance face of each slice. c) The multislice method can be considered as a two-step process.

In a STEM, the objective lens forms a narrow probe wavefunction $\Psi_p(\rho, \rho_p)$ upon the specimen surface at position ρ_p. A focused probe is usually calculated by integrating the aberration function over the objective aperture as [29]:

$$\Psi_p(\rho, \rho_p) = A_p \int_0^{q_{apr}} \exp\left[-i\chi(q) - i2\pi q(\rho - \rho_p)\right] dq, \tag{4}$$

where A_p is the normalization constant, q_{apr} is the maximum spatial frequency in the objective aperture and the function $\chi(q)$ is given by:

$$\chi(q) = \pi\lambda q^2 \left(0.5 C_S \lambda^2 q^2 + \Delta f\right), \tag{5}$$

with defocus Δf, wavelength λ, spatial frequency q in the image plane, and spherical aberration C_S. The probe is scanned across the sample and the electron intensity scattered to the angular range of the ring-shaped detector forms a convergent beam diffraction pattern (see Fig. 2). The image intensity at one point in the image is obtained by integration of the signal intensity registered by the detector. The detector function is written as $D(q) = \theta(q \in \det ector)$.

Thermal vibrations of the atoms (nuclei) result in electron-phonon (it is called thermal diffuse) scattering. An excellent approximation to include thermal diffuse scattering into the multislice method, as has been proven in Ref. [10] by a rigorous quantum mechanical phonon excitation theory, is a so called "frozen" lattice model. The basic idea behind this approach is as follows. The time necessary for high-energy electrons to pass through the specimen is about two orders of magnitude smaller than the atomic vibration period. However, for a typical beam current the atomic vibration period is much shorter than the time-interval between incoming electrons. Therefore vibrating atoms of the specimen are seen as being stationary for each incoming electron and thermal diffuse scattering can be considered as a statically averaged quasi-elastic scattering from the crystal with various configurations of static displaced atoms. Summarizing, in the "frozen" lattice model we assume that the entire crystal in one vibration configuration is a frozen lattice and the diffuse scattering generated in the whole crystal is quasi-elastic. The incoherency is introduced only at the last stage when intensities contributed by different lattice configurations are summed up incoherently.

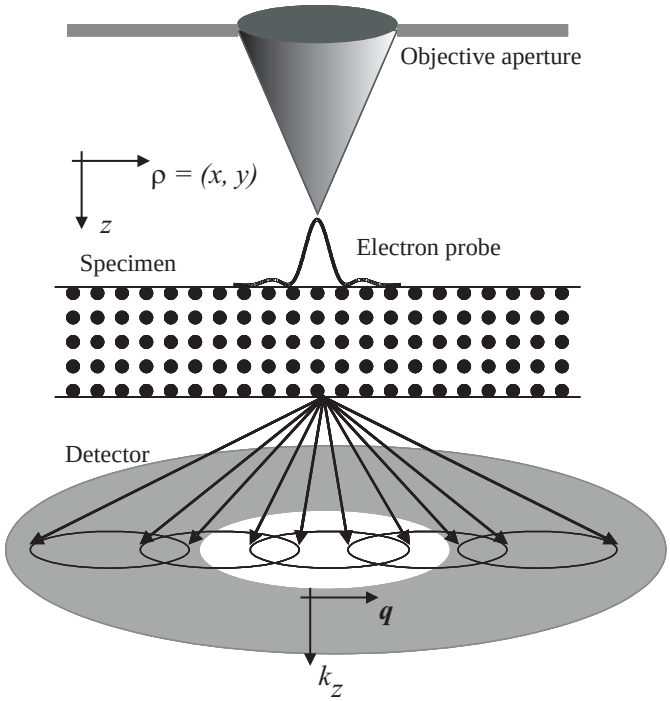

Fig. 2. Schematic diagram of ADF imaging in a STEM.

We have applied the method presented in Ref. [13, 34-36] to include the thermal diffuse scattering in the calculations. As usual, in the treatment of scattering by atomic vibrations it is assumed that TDS is not accompanied by the excitation of the electronic states in the solid and the Born-Oppenheimer approximation is adopted. If the exposure times are large (incoherent summation), the intensity distribution of the electron wavefunction in the diffraction plane is just the sum of the intensities of the inelastically (TDS wavefunction) and elastically (Bragg reflections) scattered electrons. We adopt the following notations: $\psi_0(\rho,z)$ is the independent of the crystal state wave function, obtained by averaging the electron wave function in the crystal; $\delta\psi(\rho,z,t)$ is the wavefunction, describing the inelastically scattered electrons (fluctuating part of the crystal wavefunction). Then we obtain:

$$I(q,d,\rho_p)=\left|\psi_0(q,z=d,\rho_p)\right|^2+\left|\delta\psi(q,z=d,\rho_p)\right|^2, \tag{6}$$

where d is the specimen thickness and ρ_p is a probe position. As shown in Refs. [37, 38] the perturbation or TDS potential $\delta V(\rho-\rho_k,z-z_k,t)$, which is the deviation of the instantaneous crystal potential seen by an electron at the time t from its equilibrium value, is of the same order of magnitude as the atomic potential and is considerably narrower than the averaged value of the atomic potential $V_0(\rho-\rho_k,z-z_k)$. This indicates that TDS is a localized scattering process. Therefore, the intensity of thermal diffuse scattered electrons can be written in the following form [35]

$$I_{TDS}(d,\rho_p)\approx\sigma^2\sum_{k',k''}\iint d\rho'\,d\rho''\,\hat{D}(\rho'-\rho'')\left\langle\delta U_{k'}(\rho'-\rho_{k'})\delta U_{k''}(\rho''\rho_{k''})\right\rangle\psi_0(\rho',z_{k'},\rho_p)\psi_0(\rho'',z_{k''},\rho_p), \tag{7}$$

where $\delta U_k(\rho-\rho_k)=\int\delta V(\rho-\rho_k,z-z_k,t)dz$. Here the time dependence has been dropped, because the vibration motion of the atoms is slow compared with the velocity of the incident electron and the brackets $\langle\ldots\rangle$ mean averaging over the statistical ensemble. The kernel ope-

rator $\langle \delta U_{k'}(\rho' - \rho_{k'}) \delta U_{k''}(\rho'' \rho_{k''}) \rangle$ can be generalized to the Van Hove dynamic form factor [39]. The operator $\hat{D}(\rho' - \rho'')$ is the inverse Fourier transform of the detector function $D(\mathbf{q})$.

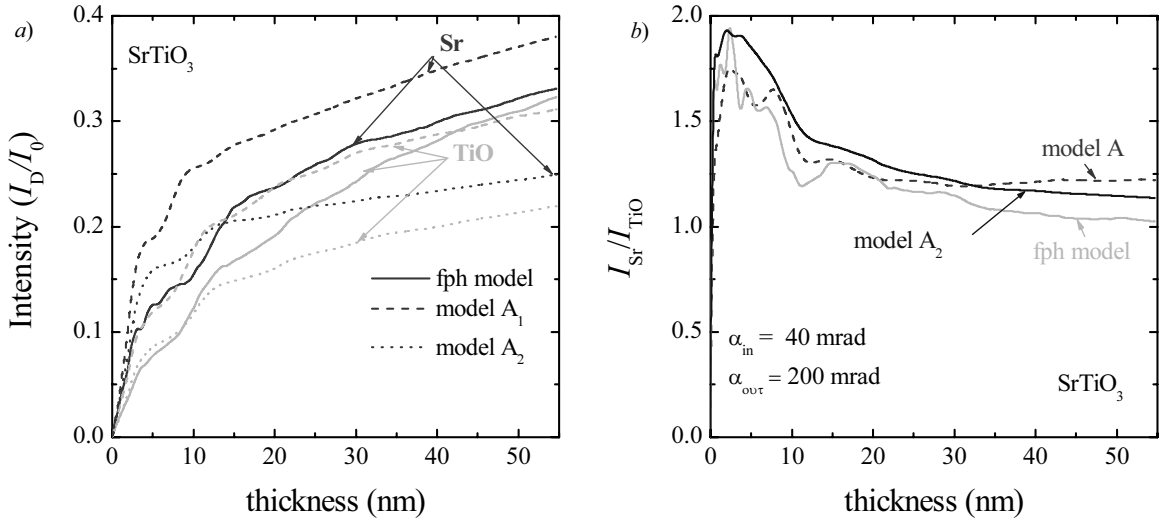

Fig. 3. a) The total (inelastic plus elastic) intensity in the annular dark field detector with an angular range 40-200 mrad for a probe located over Sr and TiO columns as a function of sample thickness. b) Intensity ratio I_{Sr}/I_{TiO} in the annular dark field detector with an angular range 40-200 mrad as a function of sample thickness.

Adopting the Einstein phonon model and assuming that the ADF detector registers all the inelastic electrons (for details, see Ref. [21], one can compute Eq. (7) numerically, since it is completely factorized

$$\begin{aligned} I_{TDS}(d,\rho_p) &\sim \sigma^2 \sum_n \int d\rho \sum_{k\in n} \left\langle \delta U_n(\rho-\rho_k)^2 \right\rangle \left|\psi_0(\rho, z_n, \rho_p)\right|^2 \\ &\approx \sigma^2 \sum_n \int d\mathbf{q} \left| G_n(\mathbf{q}) \otimes \psi_0(\mathbf{q}, z_n, \rho_p) \right|^2 D(\mathbf{q}), \end{aligned} \tag{8}$$

where

$$G_n(\mathbf{q}) \equiv FT\left[\sum_{k\in n} \sqrt{\left\langle \delta U_n(\rho-\rho_k)^2 \right\rangle} \right] \tag{9}$$

is the TDS generation function. In this expression sum is over all atoms of the *n*-th layer. The proposed approach of the calculation of the TDS intensity of the *n*-th layer is therefore somehow similar to that proposed in Ref. [17], where the TDS intensity of any layer is given by an integral over the electron density in that layer $\left|\psi_0(\rho, z_n, \rho_p)\right|^2$ multiplied with the local inelastic potential. The role of the local TDS potential is fulfilled by the square of the modified TDS generation function, which takes into account the size of the ADF detector.

In the present work we adopt the following TDS generation function, introduced in Ref. [21]

$$G_n^A(\mathbf{q}) \equiv i \sum_{k\in n} \sqrt{\tilde{a}_k^2} \left\langle \frac{\partial}{\partial x_k} U_n(\rho-\rho_k) \right\rangle, \tag{10}$$

where $\widetilde{a}_k^2$ is the two-dimensional mean vibration quadratic amplitude. Here, the summation is restricted to the atoms within one specimen slice and the intensities obtained from different slices are added incoherently. The Fourier transform of the $G_n^A(\mathbf{q})$ generation function of phonon scattering exhibits a behavior close to that of the Fourier transform of a phonon perturbation potential derived in Ref. [40].

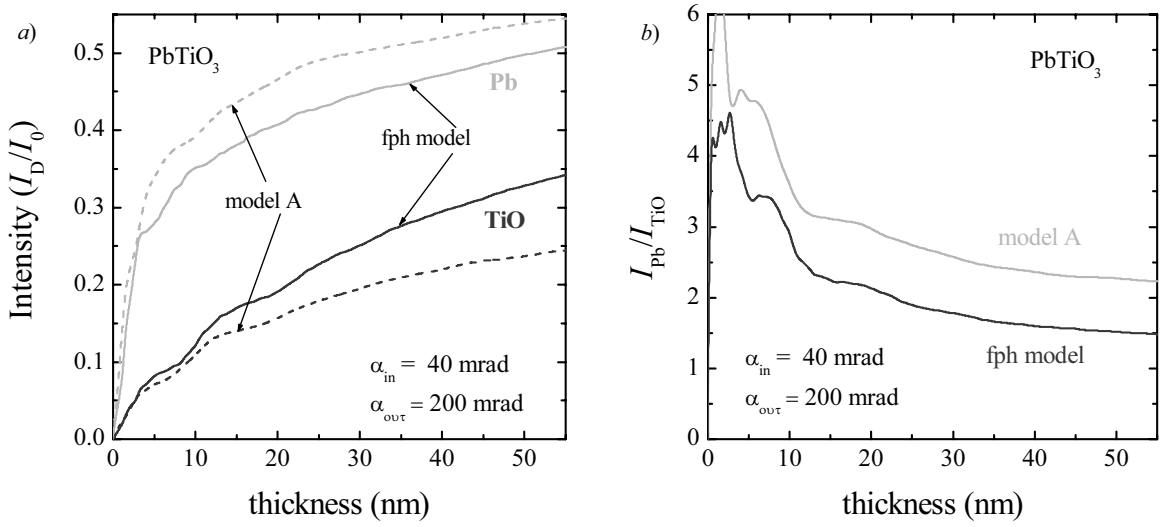

Fig. 4. a) The total (inelastic plus elastic) intensity in the annular dark field detector with an angular range 40-200 mrad for a probe located over Pb and TiO columns as a function of sample thickness. b) Intensity ratio I_{Pb}/I_{TiO} in the annular dark field detector with an angular range 40-200 mrad as a function of sample thickness.

Due to the electron-phonon scattering the intensity of the elastically scattered electrons is attenuated by the intensity of the TDS. This attenuation changes the transmission function of the multislice algorithm by the absorption potential [13]. Therefore, it should be written as

$$T_n(\rho) = \exp\left[i\sigma\left\langle U_n(\rho)\right\rangle - \mu_n^A(\rho)/2\right], \tag{11}$$

where the averaged projected potential field in the *n*-th slice is

$$U_n(\rho) = \sum_{k\in n} U_n(\rho - \rho_k) \tag{12}$$

and the absorption function $\mu_n^A(\rho)$ for the *n*-th slice have been presented in Ref. [21]. Finally, in the plane of the detector the contributions to the intensity from elastic scattering and inelastic scattering of all layers are added incoherently.

3. Results and discussion

For a numerical simulation $SrTiO_3$- and $PbTiO_3$-crystal samples have been constructed with the following geometric parameters: the transversal size is $6a_0 \times 6b_0$ (a_0 and b_0 are cell sizes in a plane perpendicular to the optic axis in the microscope) with 1024 pixels. This real space grid gives the real space sampling resolution equal to $\Delta x \approx 023$ Å/pixel. The resolution in reciprocal space is equal to $\Delta q \approx 043$ Å^{-1} and the angular resolution is equal to $\Delta\alpha = \lambda\Delta q \approx$ 0.85 mrad. This sampling restricts the calculations to the maximum detector angle of 290 mrad, which is adequate for the calculations [30]. The slice thickness is chosen as $\Delta z = c_0/4$

(Δz_{SrTiO3} = 0.97625 Å; Δz_{PbTiO3} = 0.9925 Å). STEM line images are formed by scanning a narrow electron probe along a line through the center positions of the Sr (or Pb) and TiO atomic columns. The probe is formed with an objective aperture radius of 21.27 mrad and the spherical aberration coefficient C_S is taken equal to 0.05 mm. The defocus is 115 Å (Scherzer focus) and the accelerating voltage V = 300 kV. The beam direction is chosen along the [001] zone axis. The angular detection range of the ADF detector has been chosen equal to 40-200 mrad. For the case of the $SrTiO_3$-specimen two sets of the three-dimensional atomic mean vibration amplitudes have been taken: (1) $\left(a_{Sr}^2\right)^{1/2}$=0.0486Å; $\left(a_{Ti}^2\right)^{1/2}$=0.0639Å; $\left(a_O^2\right)^{1/2}$=0.1059Å (T_D=630 K, see Ref. [41]; (2) $\left(a_{Sr}^2\right)^{1/2}$=0.0984 Å; $\left(a_{Ti}^2\right)^{1/2}$=0.0920 Å; $\left(a_O^2\right)^{1/2}$=0.1059 Å (see Ref. [42]). One set of the three-dimensional atomic mean vibration amplitudes has been taken for the $PbTiO_3$-specimen: $\left(a_{Pb}^2\right)^{1/2}$=0.0396Å; $\left(a_{Ti}^2\right)^{1/2}$=0.0765 Å; $\left(a_O^2\right)^{1/2}$=0.1269Å (T_D = 540 K, see Ref. [43]). The atomic scattering factors are used in the parameterized form taken from Ref. [30]. The calculations have been performed within frozen phonon model (fph model) and model A (for details, see Ref. [21]).

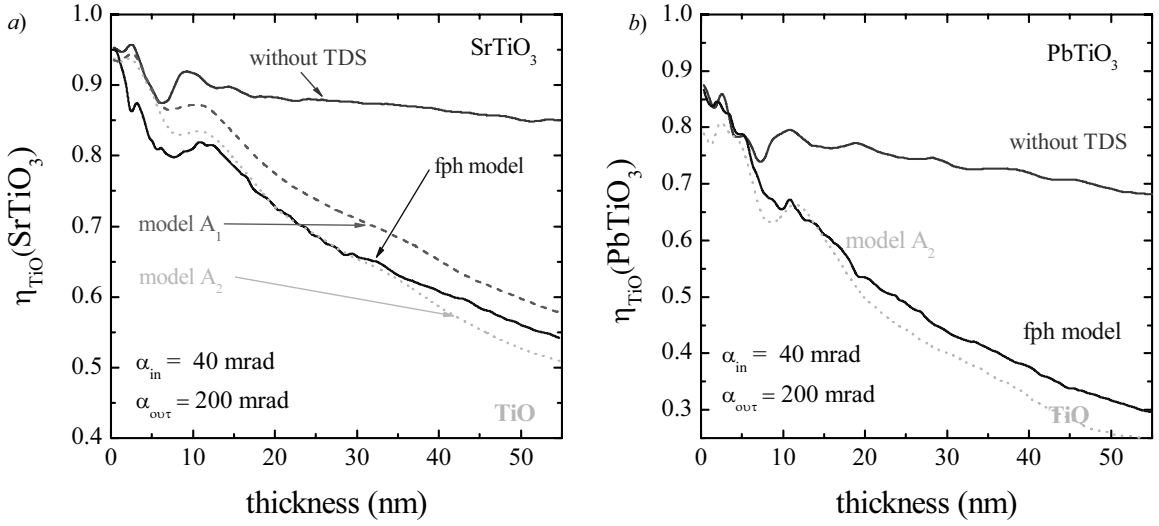

Fig. 5. The contrast of the image (TiO column) as a function of sample thickness: (a) $SrTiO_3$ crystal; (b) $PbTiO_3$ crystal.

Fig. 3(a) illustrates the thickness dependence of the simulated HAADF STEM total intensities for a [001]-oriented $SrTiO_3$-crystal, when the probe is located at the Sr and TiO atom columns. Fig. 3(b) shows the intensity ratio I_{Sr}/I_{TiO} as a function of specimen thickness. The results of the calculations based on the first set of parameters for the mean vibration amplitude exhibit slightly higher scattering intensity than those based on the frozen phonon model. Thermal diffuse scattering calculated using the second set of parameters is weaker than that obtained from frozen phonon model. In all the considered cases the intensity ration I_{Sr}/I_{TiO} shows the very close results. From Fig. 3(a) one can see that atom column intensities I_{Sr} and I_{TiO} in the $SrTiO_3$-sample increase almost monotonously with specimen thickness. There are only some weak deviations from this dependence in the region of small thicknesses. For large simulated thicknesses, the calculated intensities from both considered atom columns approach the saturation regime. This can be explained as follows. For small thicknesses the channeling of the probe electrons near an atomic column occurs. Therefore, the most of probe intensity is

focused along the column. With a thickness increase the probe wavefunction broadens and this is reflected in the simulated figure of atom column intensities I_{Sr} and I_{TiO} by a decrease of the curves' slope. Fig. 3(b) shows us that no contrast reversals occur up to 60 nm sample thickness considered in these calculations.

Fig. 4(a) displays the simulated HAADF STEM total intensity of a [001] $PbTiO_3$-crystal for the detector with annulus 40-200 mrad as a function of the sample thickness, when the probe is located over the Pb and TiO atom columns. Comparing it with the plot shown in Fig. 3(a) it is obvious that in the case of the $PbTiO_3$ sample 'saturation' of the total signal, registered when probe is located over the Pb column, occurs for smaller thicknesses. This is due to the stronger absorption of the coherent wave function, which leads to a stronger increase of the background intensity in the case of scattering from the heavier atom columns. The oscillatory behavior of the intensity is now almost suppressed and the intensity is a pure monotonic function of sample thickness. The intensity of the TiO column is also higher than that in the case of the $SrTiO_3$-sample. This is due to a larger contribution to this intensity from Pb column scattering than from Sr column in the case of the $SrTiO_3$-sample. Fig. 4(b) illustrates the intensity ratio I_{Pb}/I_{TiO} in the annular dark field detector with an angular range 40-200 mrad as a function of sample thickness. In this case the discrepancy between two considered simulation models is larger than that in the case of the $SrTiO_3$-sample.

Figs. 5(a, b) show the TiO column image contrast

$$\eta = \frac{I_{TiO} - I_{\min}}{I_{TiO} + I_{\max}} \tag{13}$$

as a function of sample thickness for $SrTiO_3$ and $PbTiO_3$ crystals. Here I_{TiO} and $I_{\min}$ are the intensity, registered when probe is located at the TiO atom column, and the minimal intensity in the line scan of an image, respectively. This figure illustrates how thermal diffuse scattering disturbs the image contrast. One can infer that in both structures the inclusion of thermal diffuse scattering in the calculations results in a strong decrease of the TiO column image contrast with sample thickness. However, this contrast loss heavily depends on the "weight" of the sample, i.e. on the atomic number of the atoms in the sample. At the same crystal thickness the reduction in image contrast is larger for the high-Z elements than for low-Z elements of the sample. Moreover, the same TiO column image exhibits a stronger contrast reduction in the case of the $PbTiO_3$ sample than that in the $SrTiO_3$ sample. For example, in the case of the detector with annulus 40-200 mrad at 550Å $SrTiO_3$ sample thickness, TDS reduces the contrast from η=0.85 to η=0.54 (frozen phonon model). In the case of the $PbTiO_3$ sample with thickness d=550Å we observe the reduction of the contrast from η=0.68 to η=0.3 (frozen phonon model), *i.e.* by a factor of more than 2.

Conclusions

In conclusion, it has been shown that inclusion of thermal diffuse scattering in the image simulation of $SrTiO_3$ and $PbTiO_3$ crystals leads to a strong reduction of the STEM image contrast. The loss of the TiO column image contrast depends on the "weight" of the sample and the sample thickness. Assuming the frozen phonon model as a reference method, we can therefore conclude that the method developed in Ref. [21] is an adequate approach to simulate thermal diffuse scattering intensity also in the case of crystalline compounds.

Acknowledgement

M.D.C. is grateful to the Fund for Scientific Research-Flanders.

References

[1] M.J. Hÿtch and W.M. Stobbs, Ultramicroscopy, 53, 191, (1994).
[2] C.B. Boothroyd and W.M. Stobbs, Ultramicroscopy, 26, 361, (1988).
[3] C.B. Boothroyd and W. M. Stobbs, Ultramicroscopy 31, 259, (1989).
[4] C.B. Boothroyd, J. Microscopy, 190, 99, (1998).
[5] C.B. Boothroyd, Ultramicroscopy, 83, 159, (2000).
[6] S. Freidrichs, J. Sloan, M.L. H. Green, J.L. Hitchison, R.R. Meyer, A.I. Kirkland, Phys. Rev. B, 64, 045406, (2001).
[7] C.B. Boothroyd, J. Electron. Micros., 51, S279, (2002).
[8] C.B. Boothroyd and M. Yeadon, Ultramicroscopy, 96, 361, (2003).
[9] P. Xu, R.F. Loane, J. Silcox, Ultramicroscopy, 38, 127, (1991).
[10] Z.L. Wang, Acta Cryst., A54, 468, (1998).
[11] Z.L. Wang and J. M. Cowley, Ultramicroscopy 31, 437 (1989).
[12] Z.L. Wang and J.M. Cowley, Ultramicroscopy, 32, 275, (1990).
[13] C. Dinges, A. Berger, H. Rose, Ultramicroscopy, 60, 49, (1995).
[14] L.J. Allen and C.J. Rossouw, Phys. Rev. B, 47, 2446, (1993).
[15] S.J. Pennycook and D.E. Jesson, Ultramicroscopy, 37, 14, (1991).
[16] K. Watanabe, T. Yamazaki, I. Hashimoto and M. Shiojiri, Phys. Rev. B, 64, 115432, (2001).
[17] L.J. Allen, S.D. Findlay, M.P. Oxley and C.J. Rossouw, Ultramicroscopy, 96, 47, (2003); L.J. Allen, S.D. Findlay, M.P. Oxley and C.J. Rossouw, Ultramicroscopy, 96, 65, (2003).
[18] C.J. Rossouw, L.J. Allen, S.D. Findlay and M.P. Oxley, Ultramicroscopy, 96, 299, (2003).
[19] A. Amali and P. Rez, Microscopy and Microanalysis, 3, 28, (1997).
[20] D.A. Muller, B. Edwards, E.J. Kirkland and J. Silcox, Ultramicroscopy, 86, 371, (2001).
[21] M.D. Croitoru, D. Van Dyck, S. Van Aert, S. Bals and J. Verbeeck, Ultramicroscopy, 106, 933, (2006).
[22] J.M. Cowley and A.F. Moodie, Acta Cryst., 10, 609, (1957).
[23] Y. Peng, P.D. Nellist and S.J. Pennycook, Journal of Electron Microscopy, 53, 257, (2004).
[24] H.A. Bethe, Ann. Phys. (Leipzig), 87, 55, (1928).
[25] D. Van Dyck, Phys. Stat. Sol. B, 72, 321, (1975).
[26] B.K. Jap and R.M. Glaeser, Acta Cryst., A34, 94, (1978).
[27] K. Ishizuka and N. Uyeda, Acta Cryst., A33, 740, (1977).
[28] D. Van Dyck, Advances in Electronics and Electron Physics, 65, 295, (1985).
[29] Z.L. Wang, Elastic and Inelastic Scattering in Electron Diffraction and Imaging, Plenum Press, New York, 1995.
[30] E.J. Kirkland, Advanced Computing in Electron Microscopy, Plenum Press, New York, 1998.
[31] D. Van Dyck, J. Microsc., 132, 31, (1983).
[32] D. Van Dyck, J. Microsc., 119, 141, (1980).
[33] D. Van Dyck, Advances in Electronics and Electron Physics, vol. 65, Academic Press, Orlando, 1985.
[34] C. Fanidis, D. Van Dyck, J. Van Landuyt, Ultramicroscopy, 41, 55, (1992).
[35] Z.L. Wang, Acta Cryst., A51, 569, (1995).
[36] C. Dinges and H. Rose, Scanning Microscopy, 11, 277, (1997).
[37] Z.L. Wang, Micron, 34, 141, (2003).

[38] Z.L. Wang, Philos. Mag. B, 79, 37, (1999).
[39] L.-M. Peng, S.L. Dudarev and M.J. Whelan, High-Energy Electron diffraction and Microscopy, University Press, Oxford, 2004.
[40] S. Takagi, J. Phys. Soc. Japan, 13, 278, (1958).
[41] S. Yamanaka, K. Kurosaki, T. Oyama, H. Muta and M. Uno, J. Am. Ceram. Soc., 88[6], 1496, (2005).
[42] W. Jauch and A. Palmer, Phys. Rev B, 60, 2961, (1999).
[43] V.G. Bhide and M.S.Hegde, Phys. Rev B, 5, 3488, (1971).